THz Imaging Radar for Standoff Personnel Screening

Ken B. Cooper, *Member, IEEE*, Robert J. Dengler, *Member, IEEE*, Nuria Llombart, *Member, IEEE*, Bertrand Thomas, Goutam Chattopadhyay, *Fellow, IEEE*, and Peter H. Siegel, *Fellow, IEEE*

(Invited Paper)

***Abstract*—A summary of the NASA Jet Propulsion Laboratory's 675 GHz imaging radar is presented, with an emphasis on several key design aspects that enable fast, reliable through-clothes imaging of person-borne concealed objects. Using the frequency-modulated continuous-wave (FMCW) radar technique with a nearly 30 GHz bandwidth, sub-centimeter range resolution is achieved. To optimize the radar's range resolution, a reliable software calibration procedure compensates for signal distortion from radar waveform nonlinearities. Low-noise, high dynamic range detection comes from the radar's heterodyne RF architecture, low-noise chirp source, and high-performance 675 GHz transceiver. The radar's optical design permits low-distortion fast beam scanning for single-pixel imaging, and a real-time radar image frame rate of 1 Hz is now possible. Still faster speeds are on the horizon as multi-beam THz transceivers are developed.**

***Index Terms*—Terahertz imaging, ultra-wideband radar.**

I. Introduction

THE problem of detecting person-borne concealed weapons or contraband from a long distance is very difficult, and no highly effective solution currently exists despite the urgent national security need. Compared to the booth-sized portal-based screening systems now in operation at many airports, a *standoff* personnel screening technology would have several advantages: At checkpoint approaches, it could provide early warning of a threat, possibly from outside the blast radius of an improvised explosive device (IED). For screening of unstructured crowds, a standoff sensor would add flexibility with its ability to point in any direction from a high vantage point. A long-range IED imager might also be easily concealed or camouflaged for covert surveillance. Its deployment in a given situation also needs to be weighed against obvious privacy concerns.

Manuscript received March 24, 2011; accepted May 20, 2011. Date of current version August 31, 2011. This work was carried out at the NASA Jet Propulsion Laboratory, California Institute of Technology, under a contract with the U.S. Naval Explosive Ordnance Disposal Technology Division, supported by the Department of Defense Physical Security Equipment Action Group and the Technical Support Working Group.

K. B. Cooper, R. J. Dengler, and G. Chattopadhyay, and P. H. Siegel are with the Jet Propulsion Laboratory, California Institute of Technology, Pasadena, CA 91109 USA (e-mail: ken.b.cooper@jpl.nasa.gov).

N. Llombart was with the Jet Propulsion Laboratory, California Institute of Technology, Pasadena, CA 91109 USA. She is now the Universidad Complutense de Madrid, Spain.

B. Thomas was with the Jet Propulsion Laboratory, California Institute of Technology, Pasadena, CA 91109 USA. He is now with Radiometer Physics GmbH, Meckenheim 53340, Germany.

Color versions of one or more of the figures in this paper are available online at http://ieeexplore.ieee.org.

Digital Object Identifier 10.1109/TTHZ.2011.2159556

THz radar imaging is a candidate technology for standoff sensing of person-borne concealed threats, and over the last four years we at the NASA Jet Propulsion Laboratory (JPL) have developed an ultra wideband 675 GHz radar [1], [2] that is capable of conducting rapid "frisk" or "pat-down" type searches of persons from a distance of 25 m as fast as once per second. The frequency band around 675 GHz was chosen because it lies in a trough of an atmospheric attenuation window, while providing sufficiently high spatial resolution for a favorable tradeoff between antenna size and standoff range. The analogy between THz radar imaging and frisking is appropriate because in both cases a hidden object is detected by its bulge underneath layers of clothing. In the radar this is accomplished by measuring with high resolution the time-of-flight (or range) that a focused, low-energy THz beam travels to the target. Because range detection is insensitive to the intensity of reflection, the specifics of the hidden object's material properties and relative orientation to the radar beam are largely irrelevant to THz radar imaging.

Besides JPL, other researchers are also making rapid progress in THz imaging radar. Near the 670 GHz window, an FMCW radar has been demonstrated primarily for industrial applications such as package inspection [3], but with the potential for person-borne concealed weapon detection as well [4]. Similar imaging radars are also being developed near the next-lower frequency transmission window at 340 GHz, where components are easier to obtain commercially and where clothing penetration and target sensitivity are higher [3], [5]–[7]. Other THz radar research is also likely underway by groups that have not yet published results, although to our knowledge no radar imaging systems have been built yet at the next *higher* transmission window near 850 GHz, where better imaging resolution will be possible at the expense of some attenuation.

In contrast to active radar imaging, passive millimeter- or submillimeter-wave standoff imaging technologies do not measure how far a hidden object protrudes from the body. Rather, they detect differences in the temperature or emissivity of a hidden object against a warm body. THz radar imaging also differs from conventional lower-frequency radars that can be used for IED detection, where radar cross section scattering metrics give a more holistic, nonimage based indication of hidden explosives on a person. For a recent reviews of the various >100 GHz technologies for concealed weapons detection, see [8] and [9]. Ultimately, given multiple and complementary detection modalities, employing a suite of different sensor technologies might be the most effective counter-IED strategy.

In this paper, we present an overview of JPL's THz imaging radar technology. The radar is currently a portable laboratory

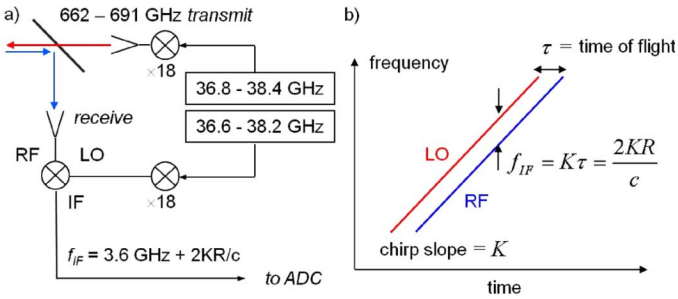

Fig. 1. (a) Schematic block diagram of the FMCW 675 GHz imaging radar employing multiplication to reach THz frequencies and stretch processing to reduce the IF bandwidth. (b) The time of flight of the radar beam to and from a target is encoded in the IF signal frequency, which is the instantaneous difference of the chirping transmitted signal and LO frequencies.

prototype system operating in a frequency-modulated continuous-wave (FMCW) mode over a 28.8 GHz bandwidth, presently centered at 676.7 GHz. With a peak output power below 1 mW, the radar is far below the relevant accepted RF or laser safety health hazard thresholds [10]–[12]. The radar can generate one $\sim 40 \times 40$ cm image per second, in real time, of targets at a standoff range of 25 ± 1 m. Many different objects concealed underneath clothing can be readily detected, including metallic guns, bomb belts, and plastic PVC pipes, as long as their size exceeds the radar's cm-scale range and cross-range resolution. The THz radar has been built largely from off-the-shelf components, but integrating them into a functioning system poses a substantial challenge. Here we will describe some key design approaches taken for the radar's detection methodology, electronics architecture, and scanning optics, which have enabled 1 s imaging times. We also demonstrate a quasi-optical time-delay two-beam multiplexer for doubling the imager's frame rate, and we outline the design of a 16-element transceiver array for reaching near video rate imaging speeds.

II. FMCW Radar Detection

A. Detected Frequency Proportional to Range

The method of FMCW radar is generally preferred over the more common pulse radar approach when the maximum power of the radiation source is too low to obtain a high signal-to-noise ratio (SNR) for short-duration pulses. This is the case for the solid state Schottky diode based frequency-multiplier THz sources we employ, which at 675 GHz produce only about 0.7 mW.

Fig. 1(a) shows a simplified block diagram of the FMCW radar approach in a THz system, where the technique of *stretch processing* is employed. In stretch processing, both the transmitted signal and the local oscillator (LO) of the receiver mixer sweep linearly over a bandwidth ΔF in time $\Delta t_{\rm chirp}$ at a rate of $K = \Delta F/\Delta t_{\rm chirp}$. We attain a transmit bandwidth of 662–691 GHz by using a $\times 18$ frequency multiplication chain fed by a K-band 36.8–38.4 GHz input source.

After reflecting off of a single target at range R, the received signal will be a near duplicate of the LO, except with a time-of-flight delay equal to $\tau = 2R/c$. See Fig. 1(b). Multiplying this temporal offset by the slope of the chirp, K, gives the frequency shift between the transmitted and received signals [the vertical distance between the lines of Fig. 1(b)]. This shift will be equal to the receiver mixer's intermediate frequency (IF) signal frequency: $\Delta f_{\rm IF} = 2KR/c$. Thus, the IF signal of the receiver mixer in an FMCW radar will have a frequency shift proportional to the range to target R. For complicated targets with scatterers at multiple ranges, the IF will contain a linear superposition of frequencies representing the different ranges.

These basic principles of FMCW radar can be found in a number of textbooks, for example [13], but to introduce notation that will be used later in a phase noise analysis, a more mathematical derivation of FMCW detection is also presented here. Let the transmitted wave amplitude versus time be represented as the complex exponential

$$S_T(t) = \exp[i\Phi_T(t)] \tag{1}$$

where the time-dependence of the chirped frequency is contained in the transmit phase function

$$\Phi_T(t)/2\pi = f_0 t + \frac{1}{2} K\, t^2 \tag{2}$$

and where f_0 is the chirp's starting frequency. After reflection from a target at range R, the received signal's phase function will be

$$\Phi_R(t) = \Phi_T(t - 2R/c) \tag{3}$$

because of the round-trip time delay. (The speed of light is c.) In the receiver mixer, this signal is multiplied with the LO signal which has a phase function similar to the transmitted signal but with an offset starting frequency, $f_0 + f_\Delta$:

$$\Phi_{\rm LO}(t)/2\pi = (f_0 + f_\Delta)t + \frac{1}{2} K\, t^2. \tag{4}$$

In Fig. 1(a), the offset frequency at the base oscillators is 200 MHz, which becomes 3.6 GHz after multiplication by 18. The IF signal's phase function will then be the difference between those in (3) and (4). (The sum signal can be ignored because it occurs at approximately twice the carrier frequency, i.e., at $675 \times 2 = 1340$ GHz, and is filtered out.) The IF signal's phase function becomes

$$\begin{aligned}\Phi_{\rm IF}(t)/2\pi &= (\Phi_{\rm LO}(t) - \Phi_R(t))/2\pi \\ &= \left(f_\Delta + \frac{2KR}{c}\right) t + \text{const.}\end{aligned}$$

where the constant term adds a time-independent phase shift that can be ignored as long as the target is stationary. For targets in motion, the dominant contribution of the constant term is just the usual Doppler-induced fractional frequency shift of twice the velocity divided by the speed of light.

Differentiating to find the IF frequency for a single target at range R yields

$$f_{\rm IF} = \frac{d}{dt}(\Phi_{\rm IF}(t)/2\pi) = f_\Delta + \frac{2KR}{c}. \tag{5}$$

Thus, apart from an additive constant f_Δ, the detected frequency shift is proportional to the range to target with a

proportionality factor of $2K/c$. Using a finite LO offset frequency f_Δ is not strictly necessary, but it is convenient for simpler IF impedance matching in the receiver mixer, lower $1/f$ noise contributions, and downstream quadrature I/Q down conversion prior to digitization.

For the 675 GHz imaging radar, the chirp bandwidth of 28.8 GHz and chirp time of 100 μs yield an IF shift of 19.2 kHz per centimeter of standoff range, or about 48 MHz at 25-m standoff. This frequency is well within the range of modern digital-to-analog converters. Had a constant-frequency LO been used instead of stretch-processing, the IF signal would have a $\sim$30 GHz bandwidth and be impractical to digitize.

B. Range Accuracy and Resolution

An important distinction in FMCW radar is the difference between the *accuracy* and *resolution* of a single measurement. The accuracy is how well the range to a *single target* can be determined. In other words, given an IF spectrum with dominant peak (or tone) from a single target, the range accuracy corresponds to the uncertainty of the peak's centroid location. This, in turn, depends on the SNR of the detected signal and the amount of signal averaging done, and it is basically independent of the peak width. Practically speaking, for bright point-targets with large SNR, the range accuracy is limited by residual motion or vibration of the radar itself, and in our system it is typically on the order of the radar operating wavelength ($\sim$0.5 mm).

However, for radar imaging of person-borne concealed weapons, the absolute range accuracy is not nearly as important as the high range *resolution* afforded by THz radar systems. The range resolution is the minimum distance that two targets can be separated along the radar's line of sight before they are indistinguishable. The reason high resolution is so important is that it allows the individual surfaces of a target's clothing, concealed objects, and body to be distinguishable from each other. This is the basis of the radar imaging approach we utilize.

The range resolution of an ideal FMCW radar depends only on the radar's bandwidth and is independent of SNR. To understand why, consider the situation of two closely spaced targets generating an IF signal composed of two nearby frequency tones. It is how well these tones can be *spectrally resolved*, i.e., the width of each tone, that determines the radar's range resolution. Thus, the minimum range resolution follows from a Fourier analysis where spectral signal widths are just the inverse of the total measurement time. The radar tone is measured for a time $\Delta t_{\rm chirp}$, and therefore the Fourier-limited single-target spectral width will be $\delta f_{\min} = 1/\Delta t_{\rm chirp}$.

Using (5) to convert from frequency to range, the minimum range resolution becomes

$$\delta r_{\min} = \frac{c \cdot \delta f_{\min}}{2K} = \frac{c}{2K\Delta t_{\rm chirp}} = \frac{c}{2\Delta F}. \tag{6}$$

All else being equal, (6) means that increasing the integration time $\Delta t_{\rm chirp}$ will not improve the range resolution because the resulting narrowing of frequency resolution is exactly canceled by the increase in the frequency-to-range proportionality factor, $c/2KR$ (5). Only the total swept bandwidth affects range resolution. The inverse relationship between range resolution and bandwidth is the same for a pulsed radar, where echoes from closely spaced targets can more easily be resolved the shorter the pulse.

The conjugate nature between bandwidth and range resolution in FMCW radar is the same as that encountered between Fourier-related variables in other wave uncertainty measurements, such as angular resolution and lens diameter in optics, or position and momentum measurements in quantum mechanics. Modern super-resolution techniques such as parametric spectral analysis might enable even finer range resolution than (6) [14], but without some reliable *a priori* knowledge of the target geometry, any improvement would likely be highly situational.

C. Chirp Nonlinearity Compensation

With a bandwidth of 28.8 GHz, the theoretical range resolution of the 675 GHz imaging radar is 5.2 mm (6), but this bandwidth-limited value is only achieved if unwanted modulation in the chirp waveform is compensated for. Our method of chirp nonlinearity compensation was first described in [15], and a more up-to-date description of the method is as follows. Consider a modulation in frequency (i.e., phase) or amplitude of the chirp waveform can be modeled as perturbations $\delta\varphi(t)$ and $A(t)$ in the transmitted and LO signals. In the THz radar, the dominant sources of $\delta\varphi(t)$ and $A(t)$ are probably the W-band power amplifiers and the submillimeter-wave multipliers above 100 GHz, which have conversion efficiencies that are not flat across the radar bandwidth, as well as frequency-dependent phase delays. The chirp source itself is generated by a custom 1.8–3.4 GHz frequency sweeper based on a direct digital synthesizer (see Section III-B), driving the front-end radar components with an extremely linear input signal.

Separate phase and amplitude modulation in the transmitted and the LO signals imparts amplitude and phase modulation on the IF signal as well, so a single point target will no longer be detected as perfect sinusoid. Rather, it becomes

$$S_{\rm IF}(t,R) = \exp[4\pi i K R t/c] A_{\rm IF}(t,R) \exp[2\pi i \cdot \delta\varphi_{\rm IF}(t,R)] \tag{7}$$

where the amplitude and phase modulation terms come from multiplying the radar signal with the receiver's LO

$$\begin{aligned} A_{\rm IF}(t,R) &= A_{\rm LO}(t) \cdot A_T(t - 2R/c), \\ \delta\varphi_{\rm IF}(t,R) &= \delta\varphi_{\rm LO}(t) - \delta\varphi_T\left(t - \frac{2R}{c}\right). \end{aligned} \tag{8}$$

The range dependence of the amplitude and phase modulation comes from the time of flight of the transmitted signal to and from the target.

For modulation that is small in strength, the IF signal of (7) will consist of a dominant tone at frequency $f_{\rm IF}$ that is broadened by the spectral width of the function $A(t)\exp[2\pi i \cdot \delta\varphi(t)]$. This broadening will degrade the radar range resolution and potentially spoil a THz radar image. To compensate for this degradation, first a calibration signal is acquired using a bright target at a range R_0 close to the radar's operating range, and the resulting IF signal is digitally stored

$$S_0(t,R_0) = \exp[4\pi i K R_0 t/c] A_0(t,R_0) \exp[2\pi i \cdot \delta\varphi_0(t,R_0)]. \tag{9}$$

All subsequent radar measurements are then divided by this calibration waveform prior to spectral analysis, so the amplitude and phase modulation of detected IF signal will be modified according to

$$A_{\mathrm{IF}}(t,R) \rightarrow \frac{A_{\mathrm{IF}}(t,R)}{A_0(t,R_0)}$$
$$\delta\varphi_{\mathrm{IF}}(t,R) \rightarrow \delta\varphi_{\mathrm{IF}}(t,R) - \delta\varphi_0(t,R_0). \quad (10)$$

The frequency of the signal will also be shifted by a known amount $2KR_0/c$ which can be added back to determine the absolute range. Insignificant range broadening will occur as long as the compensated amplitude modulation approaches unity, and the phase modulation approaches zero.

As an example, Fig. 2(a) shows the raw, uncompensated IF spectral power of a point-like target at 25-m standoff distance using the 675 GHz radar. The target is a tripod-mounted 3 inch diameter aluminum sphere, chosen for its easy and repeatable alignment to the radar beam. The wide peak near the center of the spectrum is the target, but it is severely broadened by the amplitude and phase modulation of (8).

In contrast, Fig. 2(b) shows the same measurement where the signal is first divided by a previously-acquired calibration waveform (9) prior to calculating the spectrum. The broadened peak is now a much narrower, isolated target at 25-m range. The inset of Fig. 2(b) shows the same peak (black) on an expanded scale, along with the spectrum of a numerically generated perfect sinusoid (blue) at a slightly offset range for comparison. Both signals were calculated via fast Fourier transform (FFT) using a Hann window to reduce side lobes. The fact that both have identical widths indicates that the nonlinear chirp correction procedure of (7)–(10) can totally compensate for nonlinearities in the chirp's frequency and amplitude over a dynamic range exceeding 30 dB. The observed -3 dB width of about 7 mm in Fig. 2(b) defines the radar's range resolution, and it is about 40% larger than the bandwidth-limited 5.2-mm resolution from (6) because the Hann window reduces side lobes at the expense of the main lobe width.

The peak in Fig. 2(b) is accompanied by two sidebands with strength -25 dBc, at approximately ± 1-m separation, caused by unwanted modulation picked up from some unidentified noise source in the radar electronics. For imaging they are easily filtered out. The apparent single-pulse SNR of the target in Fig. 2(b) is between 33 and 40 dB, depending on which part of the range is used to calculate the noise, but this SNR is actually phase-noise limited through a process described in Section III-C. The thermal noise floor in the absence of a target is about 25 dB lower, yielding an absolute SNR of $\sim$63 dB for the 3-in sphere target at 25 m.

Perfect compensation only occurs at exactly $R = R_0$, according to (10), where the amplitude modulation becomes unity and the phase modulation vanishes. Practically speaking, however, calibrating using a target at $R = 25$ m results in excellent nonlinearity compensation over the entire radar depth of focus of 24–26 m. This is shown in Fig. 2(c), where the 3-in spherical target is positioned at approximately 24-, 25-, and 26-m standoff and acquired using the same calibration waveform obtained at the 25-m distance. In each case, the range resolution spectral width of 7 mm is maintained, indicating perfect compensation.

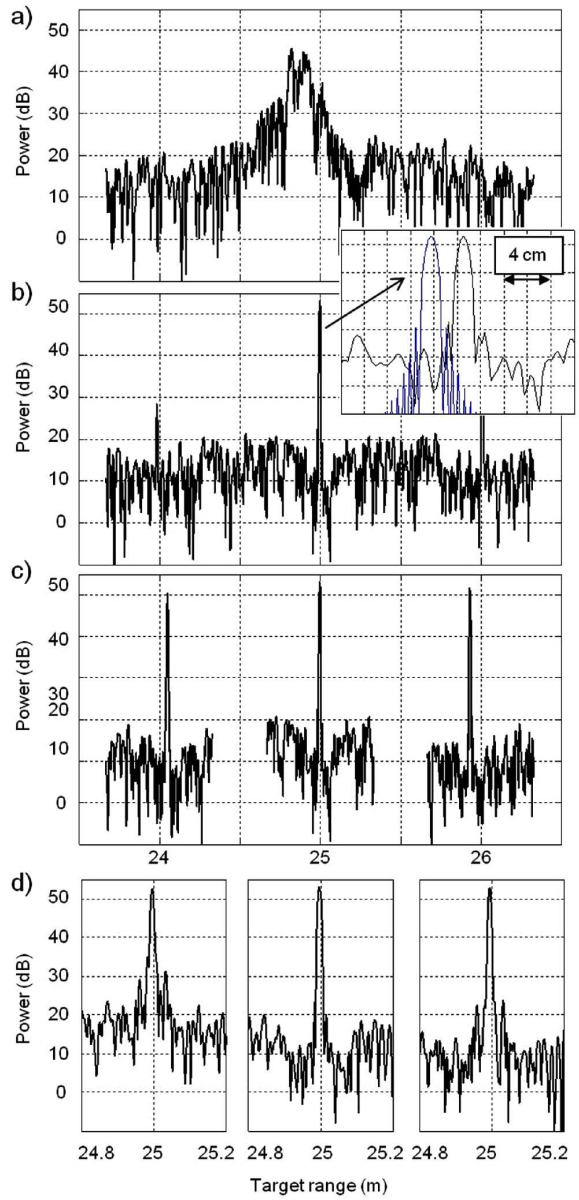

Fig. 2. (a) An uncompensated raw range spectrum of a point-like target is severely broadened by chirp waveform nonlinearities. (b) Dividing the complex IF signal by a calibration waveform focuses the range spectrum and achieves bandwidth-limited sub-centimeter resolution. (c) A single calibration waveform successfully compensates chirp nonlinearities over a wide span of target ranges. (d) At the radar power-on, the range focusing compensation is not as effective prior to the electronics warming up (left versus middle). From day to day, the warm radar does not need a fresh calibration to achieve 30 dB of dynamic range (middle versus right).

It is clear from Fig. 2(a)–(c) that good calibration is critical for achieving the highest range resolution performance, which leads to an important question for instrument practicality: How stable are the radar's nonlinearities over time? To partially address this question, Fig. 2(d) shows the range spectrum of the same 3-in sphere acquired using the same compensation vector at three different times. The plot on the left was taken immediately following the radar's power-up, before its electronics had warmed up. The middle spectrum was obtained after the radar

warmed up (about 30 minutes after power-up) and shortly following the acquisition of a fresh calibration waveform. It represents the "best possible" range spectrum of a single target. The right-hand spectrum was acquired also after the radar warmed up, but on the day following acquisition of the calibration. In all three cases, the -3 dB peak width is nearly ideal, and only for the "cold" radar is there a noticeable degradation in chirp nonlinearity compensation, visible as an increase in the lower peak width and a decrease in dynamic range. The other two spectra, obtained on different days, have largely indistinguishable characteristics over a dynamic range of about 30 dB. These results show that a single point-target calibration can provide excellent chirp nonlinearity compensation over long periods of time without the need for frequent recalibrating.

More stringent testing of the calibration stability under wider temperature excursions has not been done yet, but if this proves problematic, then there are several potential solutions to this problem. First, the radar can be easily and rapidly recalibrated by scanning the beam over a spherical target at range; however, this method might be cumbersome in a real-life operational scenario. Second, a temperature-controlled enclosure can be used for the radar electronics in a fieldable system. Third, a semitransparent screen or a small target can be placed in the radar's beam path close to the main antenna, and time-dependent changes in the signal reflected from it can be used to derive changes of errors $\delta\varphi(t)$ and $A(t)$ in real time. And finally, we have found that a typical scanned radar image of a person will contain a handful of particularly strong return signals where the beam glint off the target is very bright and dominated from a scattering region that approximates a point target. Therefore, good calibration signals may be obtainable "on the fly" as each subject is scanned, and applied to subsequent image frames to achieve the highest dynamic range possible and good spectral focusing.

III. 675 GHz Radar Electronics

A. RF Architecture Overview

The basic electronics block diagram of the 675 GHz imaging radar has changed little since we reported the first 580-GHz prototype [16], followed by a 675 GHz version [1]. The current architecture is shown in the simplified block diagram of Fig. 3, with the hardware divided into seven modules labeled by the dashed boxes A through G. Two phase-locked dielectric resonator oscillators (PLDROs) at 35 and 34.8 GHz comprise the K-band source unit (A) that drives the Tx and Rx chains. The FMCW waveform is generated by a custom fast chirp generator spanning 1.8–3.4 GHz (B), followed by upconversion onto the Tx and Rx chains units (C). These drive the front-end radar module (D), which uses a $\times 18$ harmonic frequency multiplication chain to generate the 662–691 GHz transmit beam, and a $\times 9$ multiplier chain for the 331–346 GHz LO signal pumping a subharmonic receiver mixer (SHM).

After detection, a low-noise amplifier (LNA) amplifies the IF radar signal, followed by an I-Q downconverter (E) that renders the signal complex at baseband. The 3.6 GHz LO for this mixing stage is obtained by a $\times 18$ multiplication of the 200 MHz difference frequency from the source unit A. The target signals are

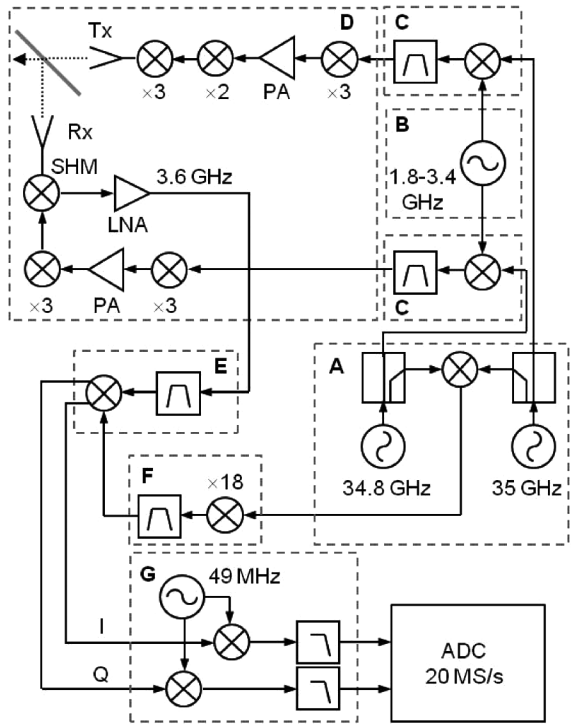

Fig. 3. Block diagram of 675 GHz imaging radar system with key RF and THz modules outlined in dashed boxes.

around 48 MHz (Section II-A), and because most of the range is target-free, only frequencies around ± 1 m of range, or ± 2 MHz in frequency centered at 48 MHz, are of interest. Therefore, a final downconversion and low-pass filter module (G) reduces the load on the analog-to-digital converter (ADC) and subsequent signal processing. The 49-MHz LO in G is generated by a programmable direct digital synthesizer (DDS), and it can be adjusted for detection at different target range centers as necessary. For added flexibility, the ADC sampling rate we use is typically around 20 MS/s, which is more than needed to capture a ± 2-MHz bandwidth. Digital downconversion, filtering, and decimation further reduces the FFT bandwidth to a ± 1-m range swath of interest.

B. Fast Chirp Synthesizer

The most significant electronics improvement of the current radar system involves increasing the speed of the low-noise chirp source [17], module B in Fig. 3. The chirper circuit is shown in the inset of Fig. 4, and it consists of an Analog Devices AD9954 DDS mounted on a custom PC board with an ADF4002 divider/phase detector to provide a reference for a separately enclosed phased-lock loop (PLL). The PLL uses a 45-MHz surface-mount LT1632 op amp in an active loop filter with a bandwidth spanning 500–900 kHz over the operating range. The 1.8–3.4 GHz voltage controlled oscillator (Mini-Circuits ROS-3800-119+) of the PLL has low phase noise and a wide fractional bandwidth with a tuning voltage range of 0–20 V. A PIC microcontroller is used to interface with the executive radar PC.

Careful digital and analog ground isolation principles were followed in the chirper design, including shielded enclosures for the PLL loop filter and power lead filtering. This reduced

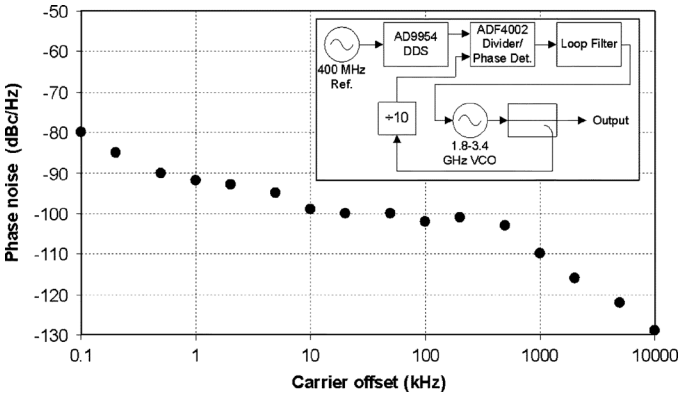

Fig. 4. A DDS/PLL hybrid synthesizer (inset) is used to generate a chirp waveform spanning 1.8–3.4 GHz in as little as 35 μs with a measured phase noise at 2.6 GHz as shown.

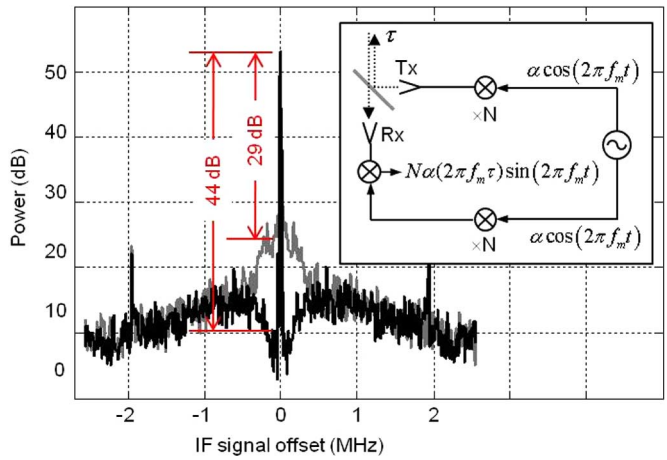

Fig. 5. Black: Point target radar spectrum showing a phase noise floor of about −44 dBc at 100-kHz offset. Gray: Same measurement when the 3.6 GHz LO of the second downconversion is generated with an uncorrelated frequency synthesizer. Inset: Principle of phase noise suppression by noise spur correlations in the RF and LO ports of a coherent receiver.

the output's spurious level below −50 dBc over nearly the entire bandwidth. Bench top tests using a length of coaxial cable in place of a radar range indicate that chirp times as short as 35 μs are achievable. The phase noise of the chirper at 2.6 GHz CW output was measured to be about −100 dBc/Hz between 10 and 100 kHz carrier offset, and lower at frequencies beyond that, as shown in Fig. 4. This is about the same level as the 35 GHz PLDROs used for the transmit and receive chains. Low phase noise is important in order to ensure high dynamic range detection; otherwise the energy of bright targets can swamp that of dimmer objects nearby in range, as described in the next section.

C. Phase Noise Cancellation

The chirper and PLDRO phase noise will add in the upconverting stage (module C in Fig. 3), and because each carries approximately the same noise level, the total increase is a factor of 2, or about 3 dB. This is followed by an additional increase of $20\log(18) = 25$ dB from the ×18 frequency multiplication in the front-end unit (module A in Fig. 3). The result will be phase noise levels of about $-100 + 3 + 25 = -72$ dBc/Hz at 100-kHz offset for both the transmitted signal and the receiver LO. With a chirp time of 100 μs, the detection bandwidth is 10 kHz (40 dB in Hz) and so the absolute phase noise floor becomes $-72 + 40 = -32$ dBc at 100-kHz offset. Because it is present at both the RF (receive port) and LO of the 675 GHz receiver mixer, the phase noise floor of a bright target would be higher by an additional 3 dB, or −29 dBc at 100-kHz offset. This is important because it will effectively limit the dynamic range of an imaging radar's ability to discern two nearby targets of different brightness.

Is the phase noise level of −29 dBc observed in practice? The black curve in Fig. 5 shows the 25-m standoff target spectrum of the same 3-in sphere used in Fig. 2, but with some additional spectral averaging to reduce noise fluctuations and with the x-axis scaled to the IF signal's frequency offset from 25 m (according to the relationship 19.2 kHz/cm). At 100-kHz offset, however, the phase noise floor is at a level of about −44 dBc, not −29 dBc as estimated above. Thus, there is a significant ∼15 dB improvement in the phase-noise limited dynamic range over this simple estimate.

The reason for this improvement is that the phase noise contributions of the PLDROs and the chirper are partially correlated in time, and therefore their fluctuations coherently subtract out, to some degree, in the mixers of the radar downconversion stages. This effect can be understood by considering the impact of a hypothetical narrowband noise spur representing phase noise at a discrete offset frequency f_m of the simplified radar circuit shown in the inset of Fig. 5. This noise spur can be written as a phase modulation

$$\delta\phi(t) = \alpha\cos(2\pi f_m t) \tag{11}$$

and for small modulation index, $\alpha \ll 1$, it will be at a power level of α^2 below the carrier.

This spur enters both the transmit and receive chains of the radar and increases by a factor of $N = 18$ (in phase deviation) after multiplication. The two spurs then reunite in the receiver mixer, where their phase magnitudes subtract by the mixing action. This phase noise cancellation would be perfect but for the unequal electrical length that each spur travels prior to mixing. In particular, the spur on the transmit branch travels round trip to the radar target and back in a time $\tau = 2R/c$. Thus, at the detection IF port of the receiver mixer, the spur signal has a phase modulation function of

$$\delta\phi_{\mathrm{IF}}(t) = N\alpha[\cos(2\pi f_m t) - \cos(2\pi f_m(t-\tau))]. \tag{12}$$

For chirp durations of 100 μs and a typical round-trip time of $\tau = 0.17$ μs for targets at 25 m standoff, the approximation $\tau \ll t$ will be valid over most of the chirp, so that a Taylor expansion of (12) in τ yields a detected spur with

$$\delta\phi_{\mathrm{IF}}(t) \approx N\alpha(2\pi f_m\tau)\sin(2\pi f_m t). \tag{13}$$

This means that the detected spur level, in power, will be reduced by the mixer cancellation effect by a factor of $(2\pi f_m\tau)^2$. This result agrees with that of a similar analysis by Shirley [18]. For $\tau = 0.17$ μs at 25-m standoff and for a modulation frequency of $f_m = 100$ kHz, the theoretical phase noise suppression will be −20 dB.

From the radar block diagram of Fig. 3, this line of reasoning applies both to the phase noise from the chirp source and from the two PLDROs. For the PLDROs, however, the phase noise cancellation occurs in the second downconversion stage (module E in Fig. 3), where the 3.6 GHz radar IF is mixed with a 3.6 GHz LO generated by mixing and multiplying by 18 the PLDRO signals. This 3.6 GHz LO input to module E has encoded in it the phase noise of both PLDROs, and these fluctuations also partially cancel upon mixing according to (13). This phase noise canceling architecture is based on the "feed-forward" tracking circuit introduced in the millimeter-wave context by Doane [19].

To test whether the theoretical phase noise suppression of -20 dB at 100-kHz offset is realized in practice, the 3-in sphere target measurement was repeated with the 3.6 GHz LO of the second downconversion stage replaced with an rack-mounted frequency synthesizer. This has the effect of eliminating the phase-noise cancellation of the two PLDROs. The result is the gray curve in Fig. 5, where a substantial phase noise penalty is observed from eliminating the feedforward tracking circuit element. At 100-kHz offset, the phase noise floor without the feedforward tracking is about -29 ± 2 dBc, compared to -44 ± 2 dBc with the 3.6 GHz feedforward LO restored. Thus, the phase noise suppression factor is seen to be around 15 ± 3 dB, which is fairly near the 20 dB estimate. In addition, the approximate frequency where the phase noise suppression should vanish is the point where $2\pi f_m \tau \approx \pi/2$. For $\tau = 0.17$ μs again, this yields $f_m \approx 1.5$ MHz, which about a factor of 3 higher than the frequency offset where the black and gray curves in Fig. 5 become identical again.

Some reasons for this moderate discrepancy with the above model include the possibility of amplitude noise effects or of a different delay time than the 50-m round-trip distance. For the latter, there could be a frequency dependence of the delay time over the chirp waveform and that is affected by asymmetric electrical lengths in the various filters, amplifiers, and multipliers in the paths to the down-converting mixers. Regardless of these details, however, the empirical evidence of Fig. 5 clearly shows that the feedforward tracking architecture significantly improves the SNR of a single-target radar response at nearby ranges. This is important for imaging applications where a weakly backscattering target would otherwise be hidden in the phase noise skirt of a brighter target. It also highlights the importance of careful RF design of active, coherent THz transceivers that confront phase noise limited performance from the use of high multiplication factors.

D. Front-End Transceiver

The radar's 675 GHz source consists of a $\times 3 \times 2 \times 3$ multiplier chain with components made by Virginia Diodes, Inc. (VDI). After the first tripler, power amplifiers at 110–115 GHz boost the signal to about 100 mW. The conversion efficiency of the final two multipliers yields an average transmit power over 660–690 GHz of about 0.5 mW, as measured by an Erickson power meter mounted to the final tripler's waveguide block. The frequency dependence of the source power across the chirp bandwidth measured in this way is shown in Fig. 6(a), where no

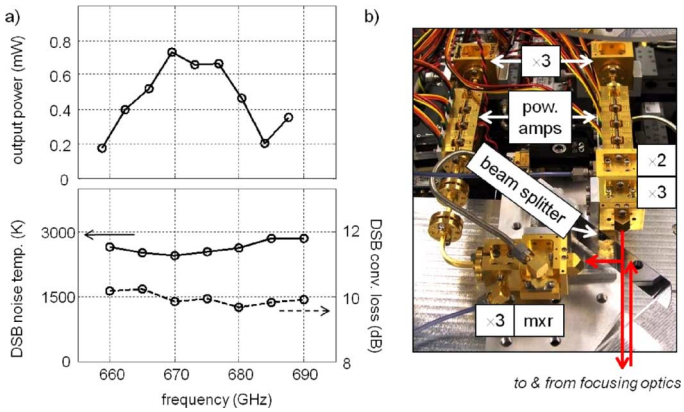

Fig. 6. (a) Transmitter output power and receiver mixer's noise temperature and conversion loss for the 675 GHz radar. (b) Photograph of the assembled radar transceiver, including a silicon beam splitter used to duplex between Tx and Rx.

correction was made for losses in the WR8-WR10 waveguide transition.

For the receiver chain, the 110–115 GHz signal drives a JPL-designed and fabricated 340 GHz tripler [20] to generate around 6 mW of LO power at 220–230 GHz. This, in turn, pumps a JPL-designed and -fabricated 675 GHz mixer based on the design of an 874 GHz mixer [21]. Both of these devices were fabricated using JPL's MoMeD process on GaAs Schottky diodes [22]. The mixer's noise temperature and conversion loss were separately measured using the Y-factor method, with the results shown also in Fig. 6(a). The chirp-averaged double-sideband (DSB) conversion loss and DSB noise temperature are 10 dB and 2600 K, respectively. A photograph of the radar transceiver's elements is shown in Fig. 6(b).

High-isolation duplexing is accomplished using a 232-μm high-resistivity silicon etalon beam splitter placed at 45° to the transmit and receive horns to achieve approximately 50/50 beam splitting [Fig. 6(b)]. On transmit, nominally half of the beam power is normally lost to a beam dump by reflection from the beam splitter, although it may also be recovered as part of a time-delay multiplexing scheme (see Section VI). Half of the beam's received energy is again lost by passing into the transmitter horn, leaving a best-case round-trip loss of 6 dB from this duplexing method. The actual duplexer loss will be worse, however, because the etalon's thickness is optimized for 50/50 beam splitting only for a p-polarized [horizontal in Fig. 6(a)] plane wave incident beam, while the actual beam diverges with a 3 dB full beam width of 10°. With these power and noise characteristics of the radar transceiver, along with the net antenna gain from the scanning optics system, we find that the SNR of human or clothed mannequin targets typically falls in the range 20–40 dB for a single 100-μs FMCW waveform.

This signal is sufficiently strong that there is no immediate need for higher sensitivity detection in the laboratory prototype system we are building. However, higher power sources, lower noise receivers, and more efficient duplexing will become more important if longer ranges or much better clothing penetration were required. A high power source could also be valuable if power splitting were used to project multiple beams on a target simultaneously. For these cases, it appears likely that advances

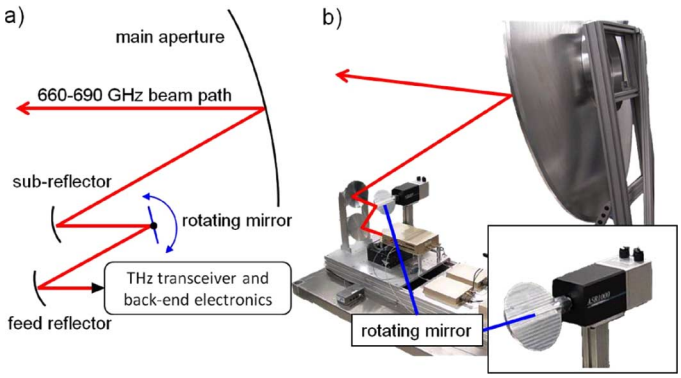

Fig. 7. (a) Schematic of beam path optics including the critical fast rotating mirror. (b) A photograph of the radar optics, along with an inset showing the fast-scanning mirror mounted on an ASR-1000 rotary stage.

in high speed transistor technology, particularly that being pioneered by Radisic *et al.* [23], will enable both low noise and power amplifiers operating at 675 GHz in the near future. Devices such as these could conceivably boost the 675 GHz radar's SNR by 10 dB or more. Another order of magnitude power increase at 675 GHz might be realized by compact vacuum electronic power amplifiers also under development now [24].

Additional SNR gain can be achieved by using a more efficient duplexer. A particularly elegant approach for this was proposed in [25], where a polarization separator (e.g., a grating or wire grid) and grating polarizer is used to convert the transmitted beam from linear to circular polarization with near-perfect efficiency. Reflection from a target changes the handedness of the beam polarization, which on reception is converted back to linear polarization but rotated by 90°. The wire grid then deflects the beam to the receiver with high efficiency. This grating/grid duplexer could increase the radar SNR by up to 6 dB compared to an ideal beam splitter. Such a duplexer is currently being tested and results will be published separately.

IV. Fast Scanning Optics

The 675 GHz radar optics have already been described in detail [26], [27]. As a brief summary, Fig. 7(a) shows a schematic diagram of the optics, along with a photograph in Fig. 7(b) of the radar platform. A 1-m-diameter main aperture focuses the beam to a (two-way) spot size of about 1 cm at 25-m standoff. Beam scanning is accomplished in the feed optics of the main reflector, where a lightweight 13-cm-diameter flat mirror is deflected over about $\pm 2.5^\circ$ in elevation and azimuth. Taking into account the overall system magnification, the corresponding beam excursion at 25-m standoff is ± 20 cm in the horizontal and vertical directions.

A system bottleneck that needed to be overcome to achieve 1-Hz imaging frame rates was the speed of the fast-scanning mirror, which deflects the beam in the vertical (elevation) direction while a slower azimuth rotary stage sweeps horizontally. The imaging frame time is determined by the scanning mirror's oscillation frequency $f_{\rm osc}$ and the number of horizontal pixels N_x according to $T = N_x/2f_{\rm osc}$. We typically image with $N_x = 50$–60 pixels and an oscillation frequency of $f_{\rm osc} = 31.25$ Hz to yield a <1-s frame time. For a peak-to-peak oscillation excursion of 5°, the corresponding angular acceleration required is 88 000°/s^2.

In addition to this fast acceleration, the angular position of the scanning subreflector must be controlled at all times to at least a precision of about 0.05°, corresponding to about half of the 1 cm on-target beam width. For our system design, it is also necessary for the motor be able to generate trigger pulses at equally spaced angles of a similar magnitude. The motor we selected is the ASR-1000 Rotary Stage made by Aerotech Corporation, shown in Fig. 7(b) with the fast-scanning reflector mounted on it. The ASR-1000 is mounted on a second slower rotary stage, the AGR-100, for azimuth scanning. The ASR-1000 consists of a servomotor and a rotary encoder, and it is driven by a model NDriveHPe motor controller. The ASR-1000 has an accuracy and repeatability better than 0.01°, a self moment of inertia of 9×10^{-5} kg m^2, and a peak torque of 5 Nm. The fast-scanning mirror is a custom-designed machined aluminum paddle that is flat on the reflecting side with a backside taper to reduce inertia. Using the calculated 3×10^{-4} kg m^2 moment of inertia of the paddle mirror plus the motor's own inertia, along with the peak torque, yields a theoretical maximum angular acceleration of about 730 000°/s^2. This is a comfortable eight times the minimum needed to achieve a 31.25-Hz oscillation frequency.

Aside from achieving high enough raw torque values, it is important that the scanning motor driver can maintain closed-loop control over the mirror oscillation at these high frequencies. This is difficult in a mechanical system because with high servo feedback gains and various self-resonances, oscillations are prone to break out. For example, a 500-Hz low-pass filter in the servo loop was required to prevent a runaway acoustic resonance of the aluminum paddle mirror, and high-gain resonant filters at the servo oscillation frequency (30 Hz) plus harmonics are required to maintain $<0.05^\circ$ angular control.

V. Concealed Object Imaging

The basic principle of THz radar image processing for concealed object imaging has been described previously [1], and it is summarized in Fig. 8(a) and (b). The radar (i.e., range) images in Fig. 8 were obtained prior to the fast-chirping synthesizer and fast-scanning mirror being integrated into the radar, and therefore they required 5 s/frame, as in [2], instead of the 1 s/frame now achievable (e.g., Fig. 9). Fig. 8(a) shows a subject standing at 25-m distance from the radar and wearing a jacket that conceals a fishing vest with three cartons of the children's modeling compound Play-Doh inside a zipped pouch. The color overlay of the photograph comprises the radar image acquired in real time over 5 s. The color scale spans 8 cm of the range to the last surface encountered by the radar beam as it scans over the target. This "back surface" is reconstructed by collecting and smoothing over the farthest peak position of each pixel's range spectrum. For example, Fig. 8(b) shows sample spectra corresponding to two different beam locations on the subject's body. Where the (THz-opaque) Play-Doh containers are snug against the jacket, the single peak detected gives the range to that peak as the back surface position. At a point mid-chest, on the other

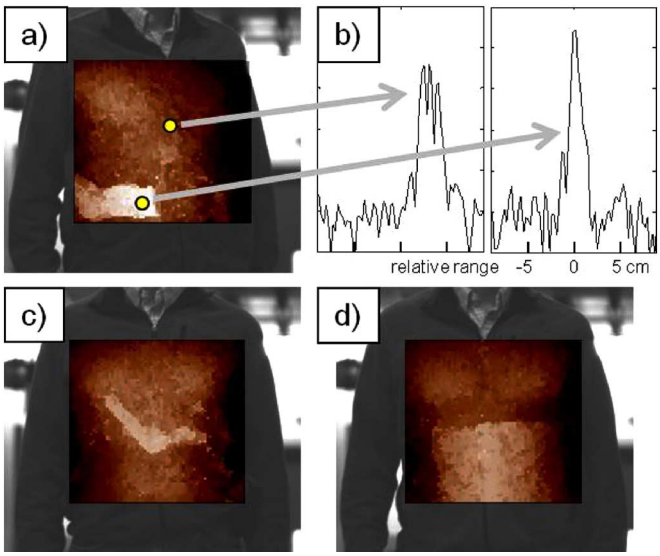

Fig. 8. (a) Radar image of a back surface revealing Play-Doh containers concealed behind a jacket. (b) Individual radar spectra corresponding to two selected points on the radar image. For multi-peaked spectra (left), the farthest peak is included in the back surface reconstruction. (c) and (d) Radar imagery revealing a hidden mock handgun and bomb belt.

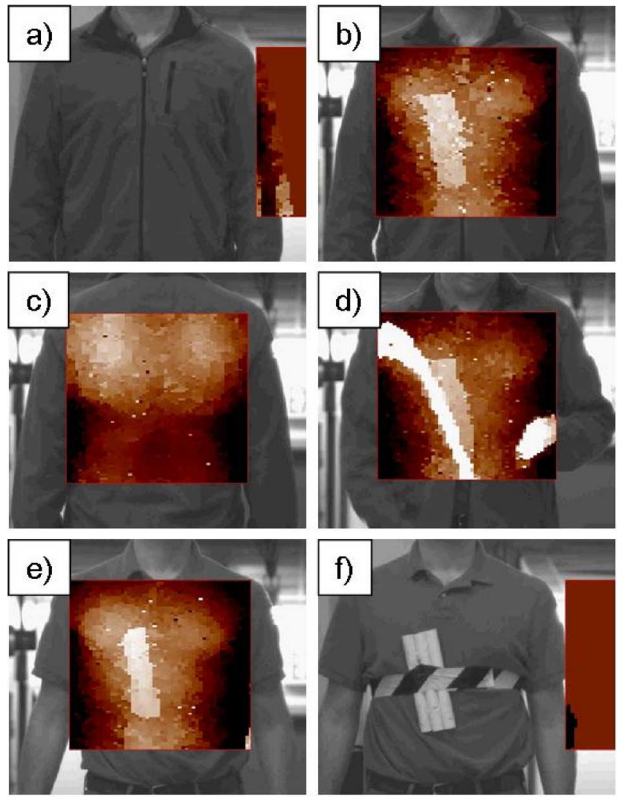

Fig. 9. Six radar images captured in a 1-Hz frame rate real-time radar imager. Visibly, there is no evidence of three 1-in PVC pipes concealed by a jacket (a). The pipes are visible when the subject moves into the radar field of view (b). No hidden objects are detected on the subject's back (c). Some image streaking (d) is a consequence of not running at video rates. With no jacket, the pipes are detected both in the radar image (e) and visibly (f).

hand, there are three clear peaks detected because of the complicated layering of the jacket, vest, shirt, and finally skin. The range to the farthest of these, presumed to be at or near the skin surface, is selected for inclusion in the back surface radar image.

Fig. 8(c) and (d), meanwhile, show that a metallic handgun and a mock bomb belt containing ceramic shrapnel and explosive stimulant can also be easily revealed with THz radar imaging. In general, any THz-opaque object can be detected as long as it is larger in size than about twice the $\sim$1 cm range and cross-range resolution.

With the faster chirper and scanning mirror, 1-s imaging times are now possible with image quality comparable to those of Fig. 8. The faster frame rates also permit video sequences of targets in motion to be made conveniently for the first time. Fig. 9 shows six stills of a 1-Hz frame rate video captured with the THz imaging radar. The elevation oscillation frequency in Fig. 9 is 31.25 Hz, and each image has 66×58 (azimuth $\times$ elevation) $=3828$ pixels. The azimuth scanning oscillation frequency is 0.5 Hz to yield a 1-s frame time. The on-target sampling density is thus about 0.6 cm per pixel, about 40% smaller than the -3 dB two-way beam width. For each $\pm 2.4^\circ$ elevation sweep, the ASR-1000 motor driver generates trigger pulses every $\sim 0.066^\circ$ in the range $\pm 2.2^\circ$. (The elevation endpoints were slightly overshot in these images to ensure all triggers were captured successfully.) With a maximum scanning velocity of 470°/s at the center of each elevation scan, the minimum time between adjacent pixels is 0.14 ms. A smaller minimum time between pixels, down to about 0.11 ms, can be tolerated for a higher pixel density or taller field of view. This lower bound is set by the 0.1 ms chirp waveform plus jitter in the elevation motor velocity.

The frame of Fig. 9(a) shows the target subject as he steps into the video camera field of view. He is wearing a cotton Polartec jacket concealing three 1 inch diameter PVC pipes taped to his torso. In the frame of Fig. 9(b), the subject has stepped into the radar imaging field of view, and the 1 second scan captures a clear, bright rectangular anomaly underneath the jacket. This is the bundle of hidden PVC pipes, which appear bright because of their protrusion away from the target's body. The radar image color scale spans 6 cm of range depth, and with a 0.7-cm radar range resolution the 2.5-cm-thick pipes are easily discriminated against the body.

In a subsequent frame shown in Fig. 9(c), the subject has turned his back to the radar, and no hidden objects are visible. In Fig. 9(d), the subject has turned to face the radar again, and during the 1-s scan shown, he has moved his right arm in a downward motion while unzipping the jacket. This motion results in a bright streak through the radar frame, although the edge of the PVC pipes is still visible. This streaking effect coming from a moving target highlights the major shortcoming of operating the imaging radar at only 1-Hz frame rates; a near-video rate radar imager would be able to resolve this motion. For the best image quality here, a target would have to be standing approximately still for 1 second. However, as Fig. 9(d) shows, some information about a concealed object is still available even when part of the frame is blurred by the subject motion. Finally, the frames of Fig. 9(e) and (f) show a radar image of the pipes with no concealing jacket, as well as the subject standing outside the radar's field of view to show the pipes in the optical image.

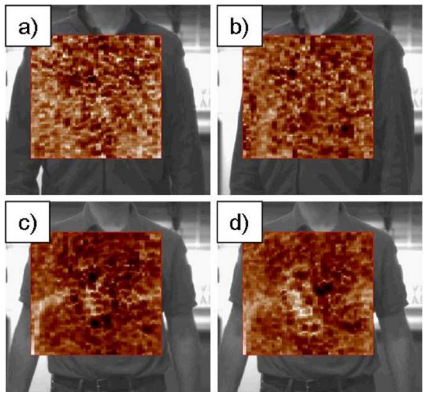

Fig. 10. (a) and (b) 675 GHz power images of a subject with jacket-concealed PVC pipes as in Fig. 9. The pipes are not detected. (c) and (d) With no concealing jacket, some signatures of the pipes are evident.

As *range images*, the pictures of Fig. 9 contain analogous information to what a "pat-down" search could reveal: lumps and bumps underneath clothing. Of course, a true pat-down would be superior in several ways, such as spatial resolution, and the human sensing of the hardness, elasticity, or texture of an object. But a THz imaging radar has the advantages of being standoff, potentially covert, and compatible with automated target recognition techniques. Also, even at 1 frame/s, which is slow compared to true video motion capture, the THz radar scan is significantly faster than a manual pat-down.

It is instructive to compare the results of Fig. 9 with some *power images* of the same target scenario, shown in Fig. 10. A power image consists of the total detected signal power over 660–690 GHz. For the data in Fig. 10, the power has been additionally range-gated over the approximately ± 1-m swath centered on the target (the integrated power over the spectral range of Fig. 2). Also, the color scale is such that darker pixels correspond to higher powers.

Fig. 10(a) and (b) shows two frames of the power image of the subject standing at slightly different angles during the video capture. The subject is wearing the same bundle of PVC pipes concealed by a jacket as in Fig. 9. However, now the pipes are not visible at all. Even though the THz radar beam penetrates the clothing, there is negligible contrast in the backscattered energy between the pipes, the clothing, and the body. Instead, the image is dominated by speckle that is characteristic for coherent imaging. Speckle comes from the large variations in the intensity of backscattered radiation coming from the diversity in angles of the beam-target incidence, and it dominates any difference in the intrinsic reflectivity of, say, PVC pipe material, clothing, and skin.

To be sure, the total dominance of speckle is not always the case. When operating in a power imaging mode, the THz radar may expose occasional "flashes" of an object being imaged. For example, Fig. 10(c) and (d) shows the power images of the same subject with the jacket removed and the PVC pipes exposed. In these two images, there is some evidence of an anomaly on the subject. In the case of Fig. 10(c), the tape around his torso appears to deflect more of the radiation than elsewhere to directions other than back to the radar aperture, therefore appearing brighter in this negative image. This is probably a result of the tape's smoothness over the THz beam size. Other portions of the pipes look dark, indicating higher intensities of backscatter. In Fig. 10(d), which shows a different movie frame with the subject turned at a slightly different angle, the pipes appear generally brighter than their surroundings, indicating smaller backscattering to the radar. Overall, however, the power images of Fig. 10 are clearly inferior in terms of concealed threat detection to the range images of Fig. 9. Moreover, this is not a very relevant situation for personnel screening because the pipes would be visible anyway in the optical camera image. It is the THz radar's unique ability to resolve closely spaced surfaces, according to (6), that underlies the basis of range-based imaging for standoff screening.

VI. Two-Beam Multiplexing and Arrays

A. Goal: Higher Speed Radar Imaging

Increasing the radar's imaging speed would prevent the blurring or streaking effects of targets in motion [e.g., Fig. 9(d)], and it would enable a larger field of view, for example a crowd of people, to be rapidly scanned over. The imaging speed our THz imaging radar is currently limited to 1 s/frame by two primary factors: the speed of the fast-scanning mirror and the SNR of single-pulse detection.

Faster scanning optics might be possible, but because a scanning motor's acceleration (or torque) scales as the inverse *square* of the imaging time, it is unlikely to be done in a cost effective manner. Fast steering mirrors based on high-speed galvanometers might provide some improvement, but reflectors of the required sizes are not off-the-shelf products and would be very expensive to develop. Off-axis spinning mirrors in various configurations might also achieve higher beam scanning velocities without huge torques [28], but achieving this in a compact volume is difficult, and the image processing would be substantially complicated by the resulting curvilinear beam scan path.

Even if faster beam scanning were achieved, the SNR speed bottleneck would also need to be overcome because a faster scanning beam means that the dwell time per image pixel decreases. For heterodyne radar detection, the SNR is directly proportional to this dwell time, and an order of magnitude frame rate speed-up would certainly degrade the radar image quality [2]. This can be compensated for by using a much higher power source (see Section III-D), but for the moment such sources are not available.

B. Time-Delay Two-Beam Multiplexing

One simple method of doubling the radar frame rate without any modifications in the scanning mechanism, source power, or back-end electronics hardware is to use time-delay two-beam multiplexing. This method was previously described and demonstrated by us in an early version of the radar which operated at 4-m standoff range and utilized a waveguide approach to duplexing [29]. We proposed an alternative all-quasioptical approach to time-delay multiplexing in [27].

The principle of the technique is summarized in Fig. 11(a), where the motivation is to "recycle" the transmitted energy that is otherwise lost to a beam dump in the fourth port of the transceiver duplexer. The first step is to divide the transmitted signal

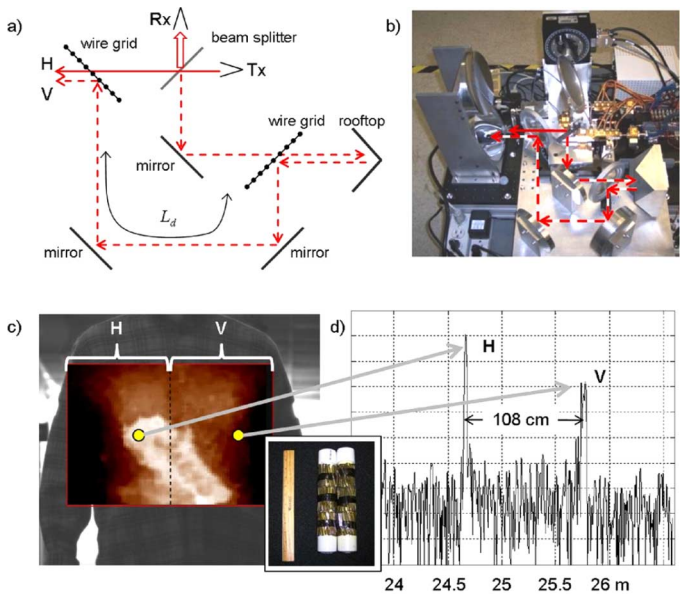

Fig. 11. Time-delay two-beam multiplexing implemented quasi-optically in the 25 m standoff radar system. (a) The "lost" transmit power through the fourth port of a duplexer is recycled in a polarization-rotating delay line and projected along with the original beam onto a target. (b) Implementation in the 675 GHz radar using additional optical components but no extra RF hardware. (c) Concealed object detection in half the time due to parallel acquisition of right and left image halves. (d) Range spectrum of a single radar waveform showing simultaneous radar detection of two different locations on a target.

power by half, for example using a beam splitter. Then one beam is allowed to pass unaffected through a wire grid oriented orthogonally to its polarization and proceeds to the radar's focusing optics and to the target. The other beam, however, is rotated in polarization and then delayed in time by propagation through a quasi-optical waveguide (i.e., free space reflectors) for a total extra path length L_d before merging with the original non-polarization-rotated, non-delayed beam using the wire grid. In a quasi-optical system, polarization rotation may be accomplished using a combination of a second wire grid and rooftop corner reflector oriented at 45° [Fig. 11(a)]. After reflection from a target, the beams retrace their original paths and then merge together at the single receiver. (Half of the power from each received beam is lost back to the transmitter and not detected, however.)

Each radar waveform would thus probe two different spots on a target simultaneously, or the same spot with two different polarizations, and the key to discriminating between the beams' signals is the relative time delay of the beams. From this delay, there will be a relative frequency shift of the polarization-rotated signal on the IF channel corresponding to a time delay $\tau = 2L_d/c$, or equivalently, a range delay of L_d. As long as L_d is much larger than any expected difference in the range from the radar to the two beam spots on the target, there will be two distinguishable peaks or clusters of peaks in the range spectra. These peaks will be easily identified by their characteristic separation by a distance L_d.

The two alternative beam trajectories can be labeled according to their transmitted polarization as H (non-delayed) and V (delayed). The original prototype of time-delay two-beam multiplexing in our previous 4-m standoff radar prototype [29] used an all-waveguide duplexer and polarization twist that caused significant ohmic loss. Also, because of the relatively low IF signal frequencies due to the short range and slow chirp rates, an elevated noise floor was observed to come from the transmitter's phase noise leaking through the hybrid coupler duplexer.

Therefore, we have chosen an all-quasioptical implementation of two-beam multiplexing in our 25-m radar system, shown in Fig. 11(b). The only hardware modifications required were the addition of six additional optical elements (two wire grids, two focusing mirrors, a flat mirror, and a rooftop reflector). The one-way delay line length of the V beam is $L_d = 94$ cm. A translation of the transceiver position by 2.3 cm was also needed to ensure the desired ~25-cm offset of the two beams' positions on the target at 25-m standoff. Additional signal power loss of the V beam coming from the delay path was measured to be only about 1 dB, and no noise floor increase from phase noise leakage was observed.

Two-beam multiplexing allows a full radar image scan to be done in half the time that a single-beam radar would take because each beam is scanned simultaneously over different halves of the field of view. As a proof of principle, an example of real-time multiplexed imaging is shown in Fig. 11(c), where a mock nail-studded pipe bomb (inset) is detected through a thick cotton flannel shirt. In this case, the H and V beams scanned the subject's right and left sides, respectively. The radar image consists of $N_x \times N_y = 80 \times 70 = 5600$ total pixels, but only $40 \times 70 = 2800$ FMCW radar pulses were required because the left and right image halves are detected simultaneously.

For example, Fig. 11(d) shows the *single* radar range spectrum acquired with the two beams simultaneously pointing at the yellow circles in Fig. 11(c). This is unlike in Fig. 8(a), where any two points on the target required two spectra to be acquired. The bright, sharp signal from the H beam corresponds to a reflection from a region near the top of the mock bomb. The second signal at a range 108 cm farther comes from the V beam intersecting near the side of the subject's body. Which beam, H or V, to associate with which peak(s) of Fig. 11(d) is obvious because this separation is nearly equal to the 94 cm of extra path length in the optical delay line. The additional 14 cm of range simply comes from range span of the target's profile across the beam spacing. Note that the V beam's signal strength is about 10 dB weaker than the H signal, probably because of the glancing angle of incidence, and its multiple peaks likely correspond to distinct reflections from the shirt and skin surfaces. This image was acquired at a point in the radar development when a 2-s single-beam scan was the radar's maximum speed, and therefore it represents a frame rate doubling from 0.5 to 1 Hz. If implemented again now, we expect that the time-delay multiplexing technique would enable 2-Hz frame rates.

Aside from shortening the scan time, the multiplexing technique can also be used for THz radar *polarimetry*. This can be done by co-aligning the H and V beams on the same region of a target. Then, any H $\rightarrow$ V or V $\rightarrow$ H conversion that occurs, for example due to the target's local geometry, will result in an IF signal corresponding to a range shift of $L_d/2$. This is because the extra path length of the time-delay element is only traversed once (either on the way out or the way back) instead of

twice. A polarimetric range spectrum will have three peaked regions; two as in Fig. 11(d), plus a third peak positioned exactly half way between them. However, our preliminary measurements suggest that no significant improvement in the power imagery (Fig. 10) is achieved using polarimetry, and that the usual range-based image contrast methods remain the most effective [30]. Nonetheless, time-delay multiplexing polarimetry might eventually find a niche in other contexts such as airborne remote sensing radars using W-band and higher frequency radars for Earth science or possibly navigation applications.

C. THz Transceiver Arrays

Time-delay two-beam multiplexing is effective for doubling a THz imaging radar's frame rate without using any additional sources, receivers, or back-end electronics. The only extra hardware required are the transceiver optics for polarization rotation and delay. Extra digital signal processing overhead is also needed to associate the detected spectral signals with the correct beam. However, for near-video rate imaging, an eightfold or higher frame rate speed-up will be necessary, and therefore a THz transceiver array would need to be used to project at least eight beams onto a target simultaneously (or four beams plus multiplexing). A "brute force" method of making an eight element THz transceiver is to build each transceiver from the individual components shown in Fig. 6(b), and then stack these together with the appropriate spacing. The resulting component would be bulky, expensive, and not easily scaled to more elements.

A superior approach that we have begun pursuing is to integrate the front-end components of a transceiver array into a monolithic stack of gold-plated silicon wafers with micromachined waveguides and device cavities. The closely spaced components in a lithographically micromachined structure will ensure low ohmic losses, and single step inter-wafer transitions can couple energy from one layer to another with low insertion loss and good matching. Recently JPL has demonstrated this approach to integrating THz components in a 560-dGHz silicon receiver module [31], resulting in an order of magnitude reduction in mass and volume.

For a radar transceiver array, Fig. 12 shows a possible 26-wafer stack for an 8- or 16-element array. (The number of elements depends on whether multiplexing is used.) Each unit cell is a dual-transceiver structure, with two 675 GHz horns per transceiver that are etched from a stack of 12 wafers (yellow). The two horns of each transceiver element are orthogonally polarized to enable time-delay multiplexing and to reduce cross-coupling. They are connected through an inter-wafer transition to two ports of a waveguide hybrid coupler serving as the radar duplexer and located in a four-wafer stack (green). All the Schottky diode devices reside in the same layer: a doubler/tripler combination for the transmitter, and a doubler/subharmonic mixer combination for the receiver. The mixer and final transmit multiplier connect directly to the hybrid coupler ports opposite the horns. Signals from the mixer's IF port are coupled through SMA connectors (pink). The next stack of four silicon wafers (red) contain 110–115 GHz MMIC power amplifiers used to drive the transmit and receive chains.

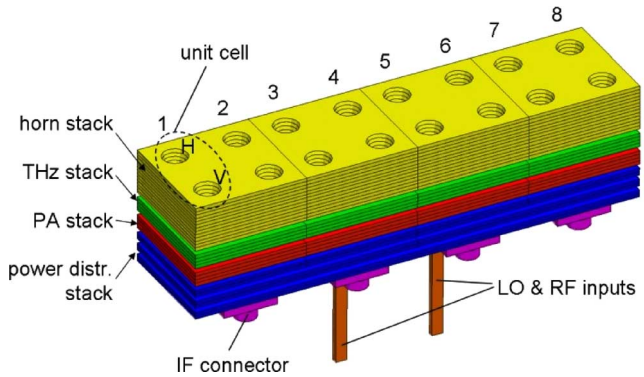

Fig. 12. A wafer stack concept for a 675 GHz transceiver array with eight pairs of orthogonally polarized transmit/receive horns for a potential 16× image frame rate speedup.

The final six wafers (blue) are used for power distribution of the two W-band source inputs (brown) for the heterodyne detection. For imaging array applications as proposed for the THz radar, integrating submillimeter-wave components in this way will prove critical for reducing the size, complexity, and cost of a multi-beam video-rate imager.

VII. Conclusion

JPL's 675 GHz imaging radar is effective as a tool for performing a rapid pat-down search from a long standoff range. At a fundamental level, this is a consequence of the radar's high three-dimensional spatial resolution and clothing penetration combining to generate digital "maps" of targets with distinguishable layers of clothing, threats, and skin. But realizing a useful THz imaging radar in the laboratory, with the potential for eventual use in the field, has required substantial engineering, development, and integration of diverse subsystems including RF electronics, THz components, optics and optomechanics, and digital signal processing. Progress in these areas, especially pertaining to fast chirp synthesis and fast-scanning mirrors, has recently led to radar imaging frame rates of 1 Hz at 25-m standoff range. Continuing progress in multi-beam target illumination and transceiver array design will further accelerate imaging speeds to near-video rates. Although this work has focused exclusively on the problem of concealed weapons detection, the underlying THz radar technology and components may also lead to innovations in other areas of remote sensing.

References

[1] K. B. Cooper, R. J. Dengler, N. Llombart, T. Bryllert, G. Chattopadhyay, E. Schlecht, J. Gill, C. Lee, A. Skalare, I. Mehdi, and P. H. Siegel, "Penetrating 3-D imaging at 4 and 25 meter range using a submillimeter-wave radar," *IEEE Trans. Microw. Theory Tech.*, vol. 56, pp. 2771–2778, 2008.

[2] K. B. Cooper, R. J. Dengler, N. Llombart, A. Talukdera, A. V. Panangadana, C. S. Peay, and P. H. Siegel, "Fast, high-resolution terahertz radar imaging at 25 meters," in *Proc. SPIE*, 2010, vol. 7671.

[3] C. am Weg, W. von Spiegel, R. Henneberger, R. Zimmermann, T. Loeffler, and H. G. Roskos, "Fast active THz cameras with ranging capabilities," *J. Infrared, Millim. Terahertz Waves*, vol. 30, no. 12, pp. 1281–1296, 2009.

[4] T. Loffler and H. Quast, "Towards real-time active THz range imaging for security applications," presented at the SPIE Eur. Defence Security Symp., Berlin, Germany, Sep. 2009.

[5] D. M. Sheen, D. L. McMakin, T. E. Hall, and R. H. Severtsen, "Active millimeter-wave standoff and portal imaging techniques for personnel screening," in *Proc. IEEE Conf. Technolo. Homeland Security*, Boston, MA, May 2009, pp. 440–447.
[6] D. M. Sheen, T. E. Hall, R. H. Severtsen, D. L. McMakin, B. K. Hatchell, and P. L. J. Valdez, "Standoff concealed weapons detection using a 350 GHz radar imaging system," in *Proc. SPIE*, 2010, vol. 7670, pp. 767008-1–767008-12.
[7] R. Arusi, Y. Pinhasi, B. Kapilevitch, D. Hardon, B. Litvak, and M. Anisimov, "Linear FM radar operating in the tera-hertz regime for concealed objects detection," in *Proc. Int. Conf. Microw., Commun., Antennas Electron. Syst.*, 2009, pp. 1–4.
[8] R. Appleby and H. B. Wallace, "Standoff detection of weapons and contraband in the 100 GHz to 1 THz region," *IEEE Trans. Antennas Propag.*, vol. AP-55, no. 11, pp. 2944–2956, 2007.
[9] H. B. Wallace, "Analysis of RF imaging applications at frequencies over 100 GHz," *Appl. Opt.*, vol. 49, no. 19, pp. E38–E47, 2010.
[10] *IEEE Standard for Safety Levels With Respect to Human Exposure to Radio Frequency Electromagnetic Fields, 3 kHz to 300 GHz*, IEEE Int. Committee on Electromagnetic Safety C95.1, 2005.
[11] *American National Standard for Safe Use of Lasers*, ANSI Z136.1-2007, Amer. Nat. Standards Inst, 2007.
[12] *Evaluating Compliance With FCC Guidelines for Human Exposure to Radiofrequency Electromagnetic Fields*, FCC Office of Engineering & Technology OET Bulletin 65, 1997.
[13] G. Stimson, *Introcution to Airborne Radar*, 2nd ed. Mendham, NJ: SciTech, 1998.
[14] M. Bouchard, D. Gingras, Y. de Villers, and D. Potvin, "High resolution spectrum estimation of FMCW radar signals," in *IEEE 7th SP Workshop on Statist. Signal Array Process.*, Jun. 1994, pp. 421–424.
[15] R. J. Dengler, K. B. Cooper, G. Chattopadhyay, E. Schlecht, J. Gill, A. Skalare, I. Mehdi, and P. H. Siegel, "600 GHz imaging radar with 2 cm range resolution," in *IEEE/MTT-S Int. Microw. Symp. 2007*, 2007, pp. 1371–1374.
[16] K. B. Cooper, R. J. Dengler, G. Chattopadhyay, E. Schlecht, J. Gill, A. Skalare, I. Mehdi, and P. H. Siegel, "A high-resolution imaging radar at 580 GHz," *IEEE Microw. Wireless Compon. Lett.*, vol. 18, no. 1, pp. 64–66, Jan. 2008.
[17] R. J. Dengler, K. B. Cooper, N. Llombart, G. Chattopadhyay, T. Bryllert, I. Mehdi, and P. H. Siegel, "Toward real-time penetrating imaging radar at 670 GHz," in *2009 IEEE MTT-S Int. Microw. Symp. Dig.*, 2009, pp. 941–944.
[18] F. R. Shirley, "FM suppression in a mix-on-self loop," *IEEE Trans. Commun. Tech.*, vol. 13, no. 4, pp. 469–475, 1965.
[19] J. L. Doane, "Broadband superheterodyne tracking circuits in millimeter-wave measurements," *Rev. Sci. Instrum.*, vol. 51, no. 3, pp. 317–320, 1980.
[20] A. Maestrini, C. Tripon-Canseliet, J. S. Ward, J. J. Gill, and I. Mehdi, "A high efficiency multiple-anode 260–340 GHz frequency tripler," presented at the 17th ISSTT 2006, Paris, France, May 2006.
[21] B. Thomas, A. Maestrini, D. Matheson, I. Mehdi, and P. de Maagt, "Design of a 874 GHz biasable sub-harmonic mixer based on MMIC membrane planar Schottky diodes," presented at the IR Millim. Wave Conf., Pasadena, CA, Sep. 2008.
[22] S. Martin, B. Nakamura, A. Fung, P. Smith, J. Bruston, A. Maestrini, F. Maiwald, P. Siegel, E. Schlecht, and I. Mehdi, "Fabrication of 200 to 2700 GHz multiplier devices using GaAs and metal membranes," in *2001 IEEE MTT-S*, 2001, vol. 3, pp. 1641–1644.
[23] V. Radisic, K. M. K. H. Leong, X. Mei, S. Sarkozy, W. Yoshida, P. Liu, J. Uyeda, R. Lai, and W. R. Deal, "A 50 mW 220 GHz power amplifier module," in *2010 IEEE MTT-S Intl. Microw. Symp. Dig.*, 2010, pp. 45–48.
[24] J. Tucek, M. Basten, D. Gallagher, and K. Kreischer, "Sub-millimeter and THz power amplifier development at Northrop Grumman," in *2010 IEEE Int. Vac. Elec. Conf.*, May 2010, pp. 19–20.
[25] J. L. Hirshfield, P. D. Kolchin, N. V. Kuzikov, and V. I. Petelin, "Quasi-optical antenna duplexer," in *25th Int. Conf. Infrared Millim. Waves*, Beijing, China, 2000, pp. 405–406.
[26] N. Llombart, K. B. Cooper, R. J. Dengler, T. Bryllert, and P. H. Siegel, "Confocal ellipsoidal reflector system for a mechanically scanned active terahertz imager," *IEEE Trans. Antennas Propag.*, vol. AP-58, no. 6, pp. 1834–1841, 2010.
[27] N. Llombart, R. J. Dengler, and K. Cooper, "Terahertz antenna system for a near video rate radar imager," *IEEE Antennas Propag. Mag.*, vol. 52, no. 5, pp. 251–259, 2010.
[28] A. H. Lettington, D. Dunn, N. E. Alexander, A. Wabby, B. N. Lyons, R. Doyle, J. Walshe, M. F. Attia, and I. Blankson, "Design and development of a high-performance passive millimeter-wave imager for aeronautical applications," *Opt. Eng.*, vol. 44, no. 9, pp. 093202-1–093202-6, 2005.
[29] N. Llombart, K. B. Cooper, R. J. Dengler, T. Bryllert, G. Chattopadhyay, and P. H. Siegel, "Time delay multiplexing of two beams in a THz imaging radar," *IEEE Trans. Microw. Theory Technol.*, vol. 58, no. 8, pp. 1999–2007, 2010.
[30] K. B. Cooper, R. J. Dengler, and N. Llombart, "Impact of frequency and polarization diversity on a terahertz radar's imaging performance," in *Proc. SPIE*, 2011, vol. 8022.
[31] B. Thomas, C. Lee, A. Peralta, J. Gill, G. Chattopadhyay, S. Sin, R. Lin, and I. Mehdi, "A 530–600 GHz silicon micro-machined integrated receiver using GaAs MMIC membrane planar Schottky diodes," presented at the 21st Int. Symp. Space Terahertz Technol., Oxford, U.K., Mar. 2010.

Ken B. Cooper (M'06) received the A.B. degree in physics (*summa cum laude*) from Harvard College, Cambridge, MA, in 1997 and the Ph.D. degree in physics from the California Institute of Technology, Pasadena, in 2003.

Following postdoctoral research in superconducting microwave devices, he joined the Jet Propulsion Laboratory, Pasadena, CA, as a Member of the Technical Staff in 2006. His current research interests include submillimeter-wave radar, spectroscopy, and device physics.

Robert J. Dengler (M'09) received the B.S. degree in electrical and computer engineering from the California State Polytechnic University, Pomona, in March 1989.

In 1988, he began his work with P. H. Siegel at the Jet Propulsion Laboratory as an intern, developing beam pattern acquisition and analysis software. Since then he has been involved in the design and construction of submillimeter-wave receivers and components, including design and fabrication of test instrumentation for submillimeter flight mixers. His recent work is focused on THz active imaging and heterodyne spectrometers, including design and construction of a 110 dB dynamic range biosample transmission imaging system at 2.5 THz, a high-resolution imaging radar system operating at 670 GHz, and an ultra high-sensitivity room-temperature 550–620 GHz absorption spectrometer.

Nuria Llombart (S'06–M'07) received the Ingeniero de Telecomunicación degree and the Ph.D. from the Universidad Politécnica de Valencia, Spain, in 2002 and 2006, respectively.

From 2002 to 2007, she was with the Defence, Security and Safety Institute of the Netherlands Organization of Applied Scientific Research (TNO), The Hague, The Netherlands. From 2007 until 2009, she was a Postdoctoral Fellow at the California Institute of Technology, Pasadena, working for the SWAT group of the Jet Propulsion Laboratory. Since January 2010, she is a Ramón y Cajal researcher at the Universidad Complutense de Madrid, Spain. Her research interests include the analysis and design of planar antennas, periodic structures, reflector antennas, lens antennas, waveguide structures, with emphasis in the THz range.

Dr. Llombart was corecipient of 2008 H. A. Wheeler Applications Prize Paper Award of the IEEE Antennas and Propagation Society. She serves as Topical Editor for the IEEE TRANSACTIONS ON THZ SCIENCE AND TECHNOLOGY and as a Member of the IRMMW-THz International Society Board.

Bertrand Thomas received the M.Sc. degree in radio communication and microwave engineering jointly from ESIEE-Paris, Paris, France, and Université Marne-la-Vallée, Marne-la-Vallée, France, in 1999 and the Ph.D. degree in astrophysics and space instrumentation jointly from the University Paris-VI, Paris, France, and Observatoire de Paris, Paris, France, in 2004.

From 1999 to 2001, he was with the Receiver Group, IRAM 30-m Radio-Relescope, Granada, Spain. From 2001 to 2004, he was with the LERMA Department, Observatoire de Paris, Paris, France. From 2005 to 2008, he was a Research Engineer with the Rutherford Appleton Laboratory, Oxfordshire, U.K., from 2008 until 2010, and he was a NASA Postdoc Program Fellow in the Submillimeter-Wave Advanced Technology Group, Jet Propulsion Laboratory (JPL), California Institute of Technology, Pasadena, working on novel silicon micromachined receiver front ends. Since 2011, he has worked at Radiometer Physics GmbH, Germany. His current research interests are the design and development of submillimeter wave heterodyne receivers for atmospheric and planetary science.

Dr. Thomas was the recipient of the 2009 JPL Outstanding Postdoctoral Research Award from NASA.

Goutam Chattopadhyay (S'93-M'99-SM'01-F'11) received the B.E. degree in electronics and telecommunication engineering from the Bengal Engineering College, Calcutta University, Calcutta, India, in 1987, the M.S. degree in electrical engineering from the University of Virginia, Charlottesville, in 1994, and the Ph.D. degree in electrical engineering from the California Institute of Technology, Pasadena, in 1999.

He is currently a Senior Member of the Technical Staff with the Jet Propulsion Laboratory (JPL), Pasadena, CA, and a Visiting Professor at the Division of Physics, Mathematics, and Astronomy at the California Institute of Technology, Pasadena, CA. His research interests include microwave, millimeter- and submillimeter-wave heterodyne and direct detector receivers, frequency sources and mixers in the terahertz region, antennas, SIS mixer technology, and direct-detector bolometer instruments.

Peter H. Siegel (S'77–M'83–SM'98–F'01) received the B.A. degree from Colgate University, Hamilton, NY, in 1976, and the Ph.D. degree from Columbia University, New York, in 1983.

He holds appointments as Faculty Associate in electrical engineering and Member of Professional Staff in biology at the California University of Technology (Caltech), Pasadena, and Senior Research Scientist and Technical Group Supervisor for Submillimeter Wave Advanced Technology (SWAT) at the Jet Propulsion Laboratory, Pasadena, CA. He has been working in the areas of millimeter and submillimeter-wave technology and applications for 35 years and has PI'd or co-I'd more than 75 R&D programs and been involved in four major space flight instruments. He has published more than 275 articles in the THz field and has given more than 75 invited talks in the United States and abroad on this subject. At JPL, he leads a group of 2 to more than 20 research scientists and engineers developing THz technology for NASA's near- and long-term space missions as well as for several DoD applications. At Caltech, he is involved in new biological and medical applications of THz. Among many other duties, he chairs the International Society for Infrared, Millimeter and Terahertz Waves (IRMMW-THz), the oldest and largest venue devoted to the field of far IR techniques, science and applications, and he served as conference organizer and chair for IRMMW-THz 2008 in Pasadena, CA. His current interests are split between traditional Earth, planetary, and astrophysics applications and new THz applications in medicine and biology.

Dr. Siegel has served as an IEEE Distinguished Microwave Lecturer, Co-Chair and Chair of IEEE MTT Committee 4—THz Technology, a TPC, Speaker's bureau and AdCom member, and as organizer and chair of seven special sessions at the IEEE International Microwave Symposia. He is extremely honored, and very excited to be involved in the formation and launching of the IEEE TRANSACTIONS ON TERAHERTZ SCIENCE AND TECHNOLOGY, for which he serves as Editor-in-Chief. His webpage is available at http://www.thz.caltech.edu.